

Eddy current damper feasibility in automobile suspension: modeling, simulation and testing

To cite this article: Babak Ebrahimi *et al* 2009 *Smart Mater. Struct.* **18** 015017

View the [article online](#) for updates and enhancements.

You may also like

- [Pulsed Galvanostatic Electrodeposition of Copper on Cobalt Using a pH-Neutral Plating Bath and Electroless Seeds](#)
D. E. Simpson, C. A. Johnson and D. Roy
- [Performance Study of a Permanent-Magnet Eddy Current Damper for Guns Recoil Control](#)
Ning Liu, Nan-nan Wang, Yan-ping Shen et al.
- [In vacuum dynamic and static tests of a thrust balance for electric propulsion with hysteresis analysis and behaviour prediction with transfer function](#)
Diogo Leon Oliveira Soares and Rodrigo Intini Marques

Eddy current damper feasibility in automobile suspension: modeling, simulation and testing

Babak Ebrahimi¹, Mir Behrad Khamesee^{1,3} and Farid Golnaraghi²

¹ Department of Mechanical and Mechatronics Engineering, University of Waterloo, Waterloo, ON, N2L 3G1, Canada

² Mechatronic Systems Engineering, Simon Fraser University, Surrey, BC, V3T 0A3, Canada

E-mail: khamesee@mecheng1.uwaterloo.ca

Received 9 July 2008, in final form 17 November 2008

Published 15 December 2008

Online at stacks.iop.org/SMS/18/015017

Abstract

This paper presents the modeling, simulation and testing of a novel eddy current damper (ECD) to be used in vehicle suspension systems. The conceived ECD utilizes permanent magnets (PMs), separated by iron poles that are screwed to an iron rod, and a conductive hollow cylinder to generate damping. Eddy currents develop in the conductor due to its relative motion with respect to the magnets. Since the eddy currents produce a repulsive force that is proportional to the velocity of the conductor, the moving magnet and conductor behave as a viscous damper. The structure of the new passive ECD is straightforward and does not require an external power supply or any other electronic devices. An accurate, analytical model of the system is obtained by applying electromagnetic theory to estimate the electromagnetic forces induced in the system. To optimize the design, simulations are conducted and the design parameters are evaluated. After a prototype ECD is fabricated, experiments are carried out to verify the accuracy of the theoretical model. The heat transfer analysis is established to ensure that the damper does not overheat, and the demagnetization effect is studied to confirm the ECD reliability. The eddy current model has 1.4 N RMS error in the damping force estimation, and a damping coefficient as high as 53 N s m^{-1} is achievable with the fabricated, scaled-down prototype. Finally, a full-size ECD is designed and its predicted performance is compared with that of commercial dampers, proving the applicability of the ECD in vehicle suspension systems.

(Some figures in this article are in colour only in the electronic version)

1. Introduction

Eddy currents are generated in a conductor in a time-varying magnetic field. They are induced either by the movement of the conductor in the static field or by changing the strength of the magnetic field, initiating motional and transformer electromotive forces (emf). The generated eddy currents create a repulsive force that is proportional to the velocity of the conductor such that the moving magnet and conductor behave like a viscous damper. The eddy current generation causes the vibration of the car frame to dissipate through the Joule heating generated in the conductor part. Applications of

eddy currents for damping purposes have been investigated for more than two decades; for example, in magnetic braking systems [1–3], the vibration control of rotary machinery [4], structural vibration suppression [5–7] and vibration isolation in levitation systems [8–10]. Sodano *et al* [5] have introduced a new electromagnetic damping mechanism to suppress a beam's vibration, where a permanent magnet is fixed so that it is perpendicular to the beam motion and a conducting plate is attached to the beam tip. In [7] a theoretical model of an ECD has been modified and developed by applying an image method to satisfy the boundary condition of zero eddy current density at the conducting plate's boundaries. An additional PM is included in the device with the like

³ Author to whom any correspondence should be addressed.

poles in close proximity, intensifying the radial magnetic flux density and enhancing the damping effect. Teshima *et al* [8] have investigated the eddy currents' damping effect on the vibration isolation properties of superconducting levitation and demonstrated that, in the vertical direction, the damping is improved by approximately 100 times by inserting ECDs into the gap between a superconductor and a magnet. Elbuken *et al* [9, 10] have proposed an eddy current damping mechanism, where a conductive plate is placed below the levitating object to suppress the vibrations and ensure stability. Such damping reduces the RMS positioning error by one-third for a 0.38 g levitated object. Schmid and Varaga [11] have designed and analyzed a vibration attenuation system for the construction of high-resolution nanotechnology structures such as a scanning tunneling microscope (STM) by using ECD. For ECD and couplers under dynamic conditions, Tonoli [12] has presented a dynamic model. Graves *et al* [13] have theoretically compared the electromagnetic dampers for a given magnetic field and material volume, based on motional and transformer emf designs. Ebrahimi *et al* [14] have developed a novel magnetic spring damper based on the eddy current damping phenomenon.

The use of electromagnetic dampers in vehicle suspension systems has drawn so much attention in recent years, due to the developments in power electronics, permanent magnet materials and microelectronic systems [15–18]. One of the main drawbacks of these electromagnetic dampers is that they are not fail-safe in the case of power failure. A passive damping element can make the active electromagnetic dampers fail-safe. The ECD has the potential to be used in electromagnetic dampers, providing passive damping for a fail-safe hybrid electromagnetic damper. Applications of the eddy current damping effect in vibration suppression studies have been reported but, to the best of the authors' knowledge, the application of eddy currents in vehicle suspension systems has not been addressed in prior publications.

This paper employs the eddy current damping effect in the development of a scaled-down damper for vehicle suspension applications. In addition, a full-size design and evaluation for an ECD applicable to vehicle suspension systems is introduced. Figure 1 depicts a schematic configuration of the proposed damper, which consists of a conductor as an outer tube and an array of axially magnetized, ring-shaped PMs, separated by iron poles, as a mover. The relative movement of the magnets and the conductor causes the conductor to undergo motional eddy currents.

An analytical approach is used for modeling the proposed device, and simulation is done using finite element (FE) analysis. The results from FE analysis and analytical models are verified by experimental studies. This paper outlines the steps taken to evaluate the proposed ECD. First, an analytical model is developed to estimate the force generated by induced eddy currents for the proposed configuration. Then, after the size of the ECD is optimized, the final geometry is modeled using the FE method. Next, the developed models together with FE results are verified by experimental studies, and the heat transfer through the conductor is investigated to complete the energy flow survey. In section 4, the design is modified for

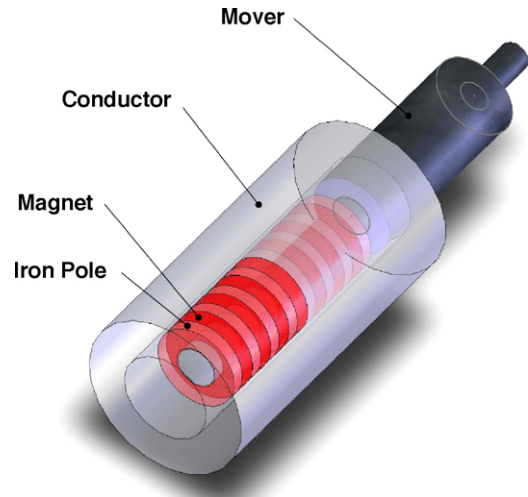


Figure 1. Schematic view of the proposed ECD.

a full-size damper, and its estimated performance is compared with that of off-the-shelf dampers. Lastly, the applicability of the ECD in vehicle suspension applications is evaluated and the demagnetization effect is studied to ensure the fail-safety and reliability of the ECD.

2. ECD design procedure

In this section, an analytical model is derived for the proposed ECD, and its geometry is optimized in order to obtain the highest damping effect for the limited external dimensions. Then, the derived model is verified by FE and experimental results. Finally, the heat transfer analysis is established to complete the energy flow investigation.

2.1. Analytical eddy current damping force estimation

Figure 2 illustrates the proposed ECD configuration. The direction of the magnetization for each PM is expressed with the bold arrow.

The assembly comprises a tubular design (figure 1), which has less leakage flux comparing to a flat design, and is vastly better for utilizing the magnetic flux, leading to higher eddy current generation. Axially magnetized PMs in the mover result in a higher specific force capability than that of radially magnetized ones. Annularly shaped magnets, supported by a non-ferromagnetic rod, are selected instead of disc-shaped magnets, and fastened on a nonmagnetic rod, reducing the effective air-gap. Due to the relative motion of the PMs, eddy currents are generated in the conductor.

The eddy current phenomenon occurs either in a steady conductor in a time-varying magnetic field, or in a conductor that moves in a constant magnetic field. The former contribution is associated with the *transformer* eddy current and is calculated by the third Maxwell equation (Faraday's law), whereas the latter is associated with the *motional* eddy current and is calculated by the Lorentz force law. The total

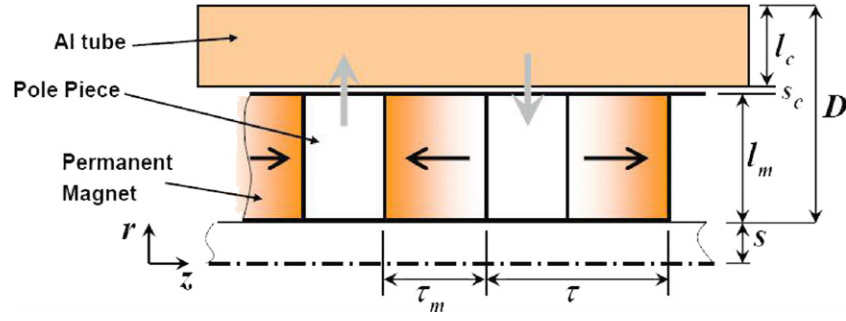


Figure 2. Configuration of the proposed ECD.

induced emf is expressed by computing

$$E = E_{\text{trans}} + E_{\text{motional}} = - \int_s \frac{\partial \mathbf{B}}{\partial t} \cdot d\mathbf{s} + \int_c (\mathbf{v} \times \mathbf{B}) \cdot d\mathbf{l}, \quad (1)$$

where \mathbf{v} and \mathbf{B} are the relative velocity of the magnetic flux and conductor, and the magnetic flux density, respectively. If the magnetic flux density is constant, the induced current density \mathbf{J} in the conducting sheet is calculated due to the motional eddy current as follows:

$$\mathbf{J} = \sigma(\mathbf{v} \times \mathbf{B}), \quad (2)$$

where σ is the conductivity. The induced current density creates a magnetic field that opposes the effect of the external applied magnetic field and causes a damping force in the z direction, which is simplified in [5] as

$$\mathbf{F} = \int_{\Gamma} \mathbf{J} \times \mathbf{B} d\Gamma = -\hat{k}\sigma(\tau - \tau_m)v_z \times \int_0^{2\pi} \int_{r_{\text{inside}}}^{r_{\text{outside}}} r B_r^2(r, z_0) dr d\theta, \quad (3)$$

where Γ , r_{inside} and r_{outside} are the conductor's volume, inside radius and outside radius, respectively. τ and τ_m are the pole pitch and the magnets' thickness. In conclusion, the equivalent constant damping coefficient, C , for the proposed configuration is obtained as

$$C = \sigma \int_{\Gamma} B_r^2 d\Gamma. \quad (4)$$

Figure 3 depicts the schematic configuration of the PMs in the proposed design. Among different proposed approaches for calculating the magnetic flux density of a magnet [19], the model proposed by Craik [20] is used for the magnetic flux density calculations as it offers an accurate model with a reasonable complexity. For a PM with length τ_m and radius R , the magnetic flux density at distance (r, z) from the PM geometric center is obtained by computing

$$B_r(r, z)|_{R, \tau_m} = \frac{\mu_0 I}{2\pi \tau_m} \int_{-\tau_m/2}^{\tau_m/2} \frac{(z - z')}{r [(R + r)^2 + (z - z')^2]^{1/2}} \times \left[-K(k) + \frac{R^2 + r^2 + (z - z')^2}{(R - r)^2 + (z - z')^2} E(k) \right] dz'. \quad (5)$$

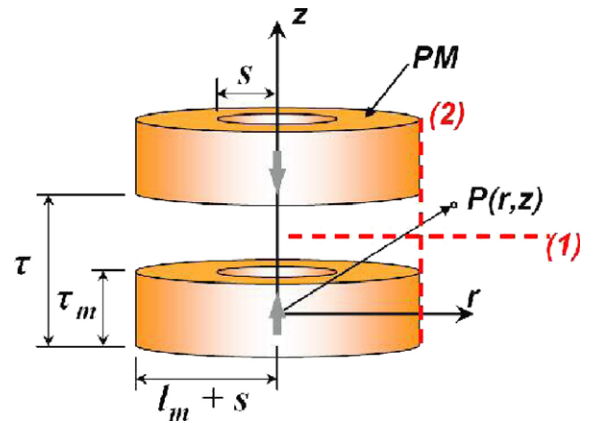


Figure 3. Schematic view of two PMs with like poles in close proximity.

$K(k)$ and $E(k)$ are the complete elliptic integrals of the first and second kind, respectively, and are defined as

$$K(k) = \int_0^{\pi/2} \frac{d\theta}{\sqrt{1 - k^2 \sin^2 \theta}} \quad (6)$$

and

$$E(k) = \int_0^{\pi/2} \sqrt{1 - k^2 \sin^2 \theta} d\theta, \quad (7)$$

where

$$k^2 = 4Rr[(R + r)^2 + (z - z')^2]^{-1}.$$

$I = M\tau_m$ is the equivalent current of the PM [21]. For the PMs, the axial magnetic fluxes, along dashed line 1 in figure 3, cancel each other, whereas the two radial fields are combined to produce a radial magnetic flux that is exactly twice as high as the one produced by a single magnet. Therefore, the total radial component of the magnetic flux density, B_r , along dashed line 1 is given by

$$B_r = 2(B_r(r, z)|_{l_m+s, \tau_m} - B_r(r, z)|_{s, \tau_m}). \quad (8)$$

Since (5) does not have any analytical solution [5], a numerical approach is adopted for solving the integrals, and the estimated values are validated by both experimental as well as FE results. The comparison of the results is shown in figure 7.

Equation (3) is modified to accommodate the skin effect. This effect is the tendency of an alternating current in a

conductor to be distributed such that the current density at the conductor surface is greater than the density at the core. The skin effect causes the effective, conductor's resistance to increase with the current frequency. The current density in a thick conductor plate decreases exponentially with depth d from the surface, represented by

$$J = J_s e^{-d/\delta_p}, \quad (9)$$

where J_s and δ_p are the current at the surface and the depth of penetration, respectively. The depth of penetration is defined as the depth below the conductor surface at which the current density decreases to $1/e$ of the current at the surface, and is obtained from

$$\delta_p = \sqrt{\frac{1}{\sigma \pi \mu f}}, \quad (10)$$

where f is the frequency of the alternating current and μ is the absolute magnetic permeability of the conductor equal to $\mu_0 \mu_r$ (μ_r is the relative permeability of the conductor). Equation (3) is modified to accommodate the described skin effect as follows:

$$F = 2\pi \sigma (\tau - \tau_m) v_z \int_{r_{\text{inside}}}^{r_{\text{outside}}} r B_r^2 e^{\frac{-(r-r_{\text{inside}})}{\delta_p}} dr. \quad (11)$$

Equation (11) is computed for the damping force estimation of the proposed ECD configuration.

2.2. Sizing of the proposed topology

This section is concerned with the initial sizing of the scaled-down damper, for proof of concept and verification of the analytical and FE models. The geometry of the proposed ECD is optimized to obtain the highest damping force, regarding the external and internal dimension restrictions. The conductor external radius ($D + s$), inner rod radius (s) and air-gap thickness (s_c) are selected as 25 mm, 6.25 mm and 0.5 mm, respecting the external size constraint, mechanical stress consideration and manufacturing restrictions, respectively. The conductor thickness (l_c) is obtained such that it is equal to the eddy current depth of penetration at the highest working frequency. For the study in this paper, the depth of penetration at 30 Hz is obtained from (10), 12 mm. By considering the restricted external diameter and $l_c = 12$ mm, the ring-shaped magnets' diameter ($2(l_m + s)$) of each magnet is calculated as 25 mm. The outward magnetic flux from each pole is estimated by

$$\phi_g = 2\pi (l_m + s) (\tau - \tau_m) B_r, \quad (12)$$

where B_r is calculated from (8). Figure 4 reflects the variation of this outward magnetic flux in terms of the normalized magnetic thickness.

It is observed that the maximum flux is obtained at τ/τ_m equal to 0.55. Consequently, the magnets' thicknesses have an optimal value of 5 mm by assuming the pole pitch τ is 9 mm. After the ECD dimensions are designed to obtain the highest radial flux in the air-gap, and thus the highest damping force, an experimental analysis is conducted in the next sections and the results are employed to validate the derived model.

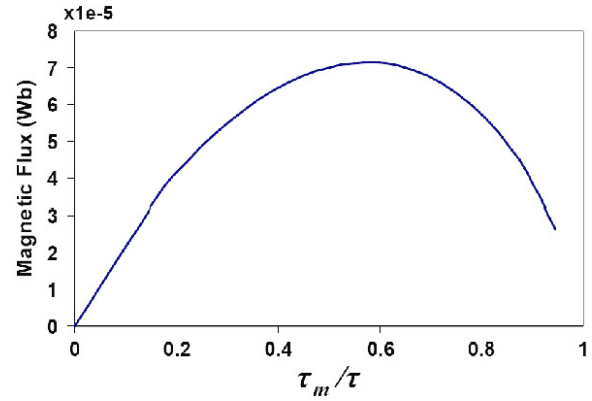


Figure 4. Magnetic flux versus normalized magnet thickness.

Table 1. ECD prototype dimensions.

Item/symbol	Value/unit
Number of poles p	8 poles
Air-gap s_c	0.5 (mm)
Pole pitch τ	8 (mm)
Conductor external radius $D + s$	25 (mm)
Magnets' thickness τ_m	5 (mm)
Conductor thickness l_c	12 (mm)
Rod diameter $2s$	12.5 (mm)
Magnets' material	NdFeB alloy
	$B_r = 1.17$ (T)
Magnets' diameter $2(l_m + s)$	25 (mm)

2.3. Finite element modeling

A two-dimensional axisymmetric model of the damper is simulated, using Comsol-Multiphysic 3.3, for further analysis of the proposed ECD and to estimate the magnetic flux density. Figure 5 shows the 2D model of the proposed mover configuration. Magnetic flux density streamlines and the induced magnetic field are plotted in this figure.

It is observed that the radial magnetic flux density is concentrated and enhanced at the iron pole pieces, causing more eddy current induction such that the ECD is more effective. After the FE model verification by both analytical and experimental results in section 2.4, it will be used for the flux density estimation in the real-size ECD design in section 3.

2.4. Experimental set-up for magnetic flux measurements

After the size is optimized in section 2.2, a prototype ECD is fabricated and experiments done to verify the accuracy of the analytical model for the magnetic flux density (8) as well as the force model (11). Figure 1 provides a schematic view of the novel ECD, which is fabricated and tested. Its dimensions are obtained in section 2.2 and listed in table 1.

Figure 6 denotes the experimental set-up, which is used for magnetic flux measurements. The gaussmeter (LS410) is used to measure the magnetic flux density. The gaussmeter probe is moved to the desired position by an Epson SCARA robot. The radial magnetic flux density is measured in 0.5 mm steps along the mover's length.

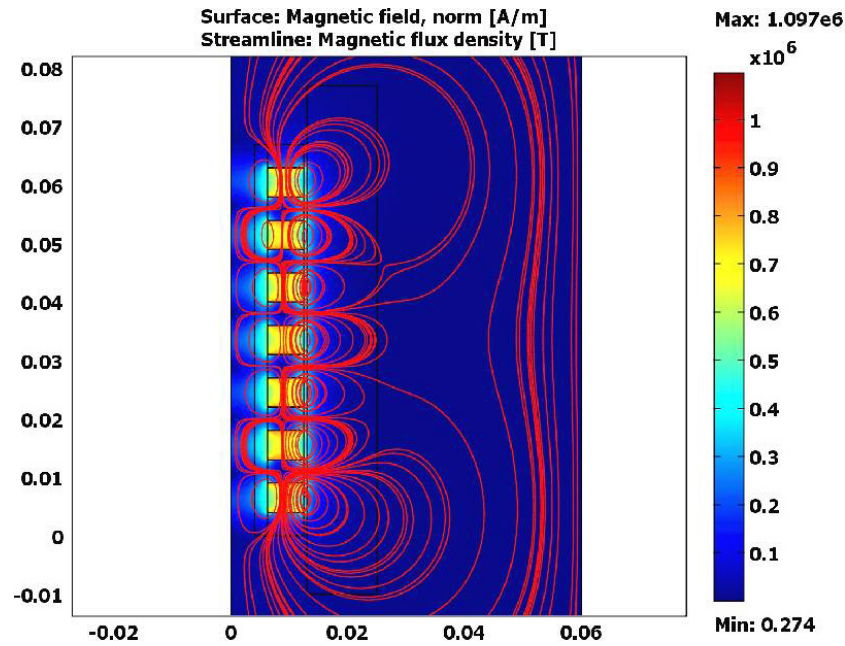


Figure 5. 2D axisymmetric FE simulation of the scaled-down prototype.

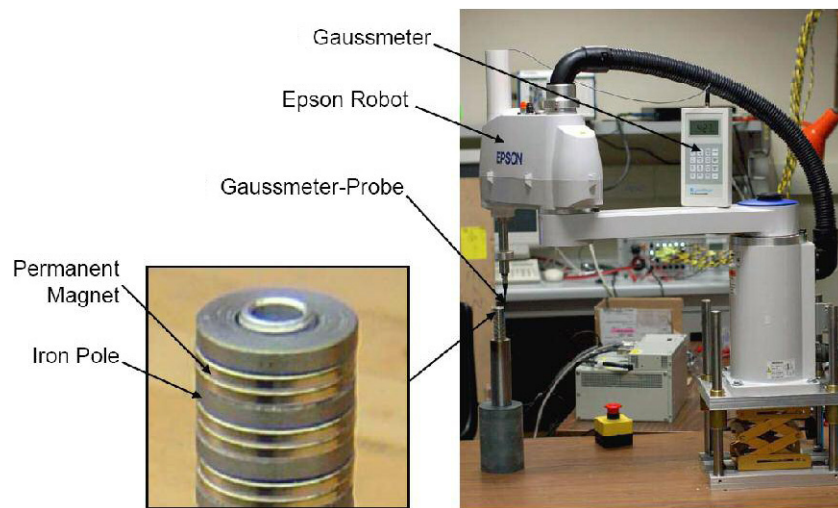


Figure 6. Experimental set-up for magnetic flux measurements.

Figure 7(a) exhibits the radial component of the magnetic flux density along horizontal line 1 in figure 3 at the mid-distance between PMs, obtained from analytical as well as FE results. In addition, the FE results are verified by the experimental results for the case in which the iron pole is inserted between the two magnets. The magnets and the conductor boundaries are added, providing more clarity. The data are captured from the pole surface at $r = 12.5\text{--}25\text{ mm}$. Although the insertion of an iron pole between the two magnets causes a 50% increase in the flux at the magnets' edges, the iron pole effect decreases as the distance from the magnets increases in a way that the maximum flux change in the conductor is not more than 2%. Thus, the derived analytical calculations are still valid, estimating the generated force in the conductor due to eddy currents. It is also concluded that the analytical model has less than 0.02 T (6%) error in estimation

of the radial flux density. Figure 7(b) shows the radial flux density along vertical dashed line 2 in figure 3. It is evident that the analytical approach accurately models the flux density. The calculated magnetic flux density is used for the eddy current estimation.

2.5. Experimental set-up for dynamic force measurements

To validate the accuracy of the force model (11), another experimental set-up is established. As shown in figure 8, the experimental test bed consists of an LMS 722 electromagnetic shaker, which is controlled by an accelerometer sensor feedback. An A/D board captures the data from the load cell, which is set firmly in place, and the linear variable displacement transducer (LVDT). The measurements are taken at the University of Waterloo.

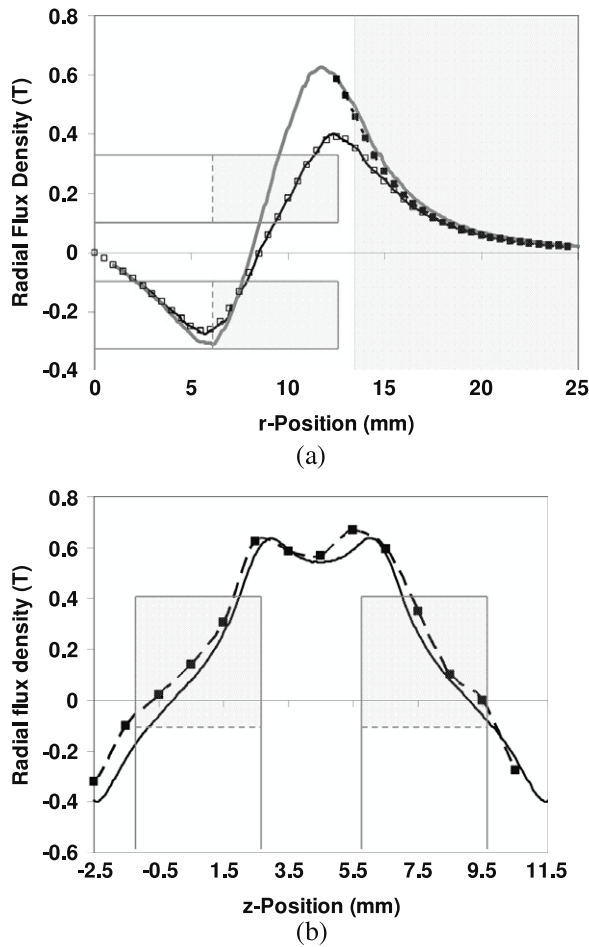


Figure 7. Radial component of the flux density, (a) along line 1 obtained from: \square : analytical, $—$: finite element, $—$: finite element (with iron pole), \blacksquare : experiments (with iron pole), and (b) along line 2 in figure 3 obtained from: $—\blacksquare$: experiments, and $—$: finite element analysis.

The measurements are carried out at the constant amplitude of 2 mm and a frequency range of 5–45 Hz. Figure 9 represents the dynamic behavior of the scaled-down ECD prototype at various frequencies.

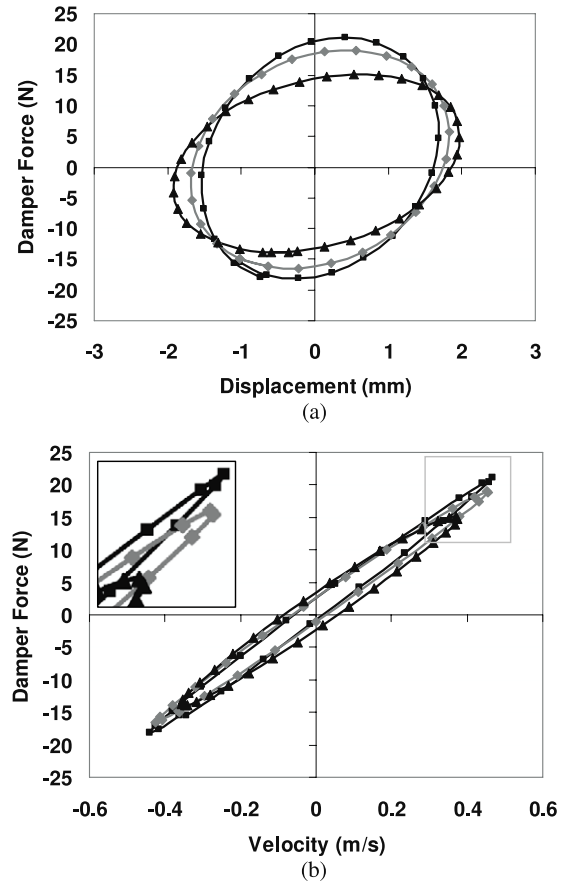


Figure 9. (a) ECD force versus displacement and (b) ECD force versus velocity at \blacksquare : 45 Hz, \blacklozenge : 40 Hz, \blacktriangle : 30 Hz.

Another vital graph for the dynamic characterization of a damper is the peak force with regards to the peak velocity. As observed in figure 10, the results from the experimental analysis are in good agreement with those of the analytical model in (11); for the model without the skin effect consideration, the damping force appears to be overestimated. The derived model for the damping force exhibits 1.4 N (7%) RMS error in the damping force estimation. To validate the derived model for the eddy current damping force, the next

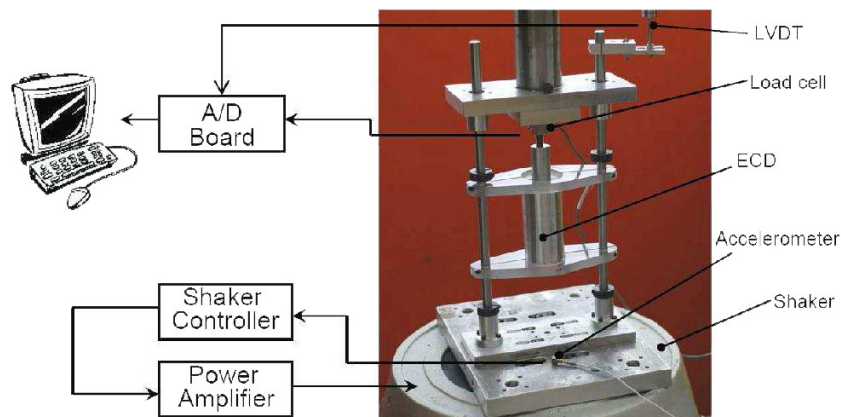


Figure 8. Experimental set-up for ECD.

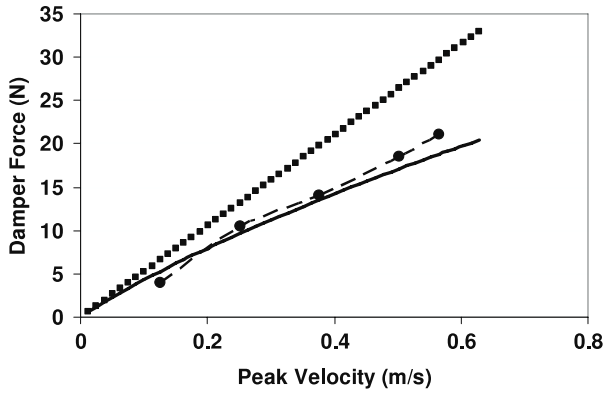


Figure 10. ECD peak force versus peak velocity at a constant amplitude of 2 mm. —●—: experimental, —: analytical with skin effect, and ---: analytical without skin effect.

step is to analyze the ECD from the heat transfer perspective and to estimate the temperature rise due to the eddy current generation in the conductor material.

2.6. Heat transfer analysis

As discussed earlier in section 1, the vibration energy of the car frame is converted into heat via eddy current induction causing the conductor to heat up. The primary role of this section is to establish the heat transfer properties of the damper to ensure it does not overheat and to predict the temperature rise to be used in PM demagnetization studies in section 4.1.

In this section, after the governing heat transfer equations for the ECD are derived, the temperature increase due to the eddy current generation at the inside surface of the conductor is calculated. The heat is generated around the internal surface of the conductor cylinder and is dissipated either by the forced convection in the air-gap and then by the conduction in the mover, or by the natural convection at the external surface of the conductor. A schematic view of the thermal resistance network for the ECD heat transfer is given in figure 11.

By calculating the thermal resistances, the surface temperature is obtained from Newton's law of cooling as follows:

$$(T_s - T_\infty) = \left[\frac{(R_{\text{Cond}} + R_{\text{N.Conv}})(R_{\text{F.Conv}} + R'_{\text{Cond}} + R'_{\text{F.Conv}})}{R_{\text{Cond}} + R_{\text{N.Conv}} + R_{\text{F.Conv}} + R'_{\text{Cond}} + R'_{\text{F.Conv}}} \right] Q. \quad (13)$$

The conduction resistances are conveniently obtained as

$$R_{\text{Cond}} = \frac{\ln(r_3/r_2)}{k_c 2\pi L} \quad (14)$$

and

$$R'_{\text{Cond}} = \frac{\ln(r_1/s)}{k_m 2\pi L}, \quad (15)$$

where k_c and k_m are the thermal conductivity of the conductor and mover, respectively. The forced-convection resistances are found by computing

$$R_{\text{F.Conv}} = \frac{1}{h_F (2\pi r_2 L)} \quad (16)$$

and

$$R'_{\text{F.Conv}} = \frac{1}{h'_F (2\pi s L)}, \quad (17)$$

where h_F and h'_F are the forced-convection heat transfer coefficients, calculated from

$$h_F = \frac{k_a}{s_c} Nu \quad (18)$$

and

$$h'_F = \frac{k_a}{2s} Nu, \quad (19)$$

where k_a and Nu are the thermal conductivity of the air and the Nusselt number, respectively. The dimensions, s_c and $2s$, represent the characteristic lengths (L_c s) of the respective geometries. The Nusselt number is calculated from empirical equations [22] and depends on the flow regime. The

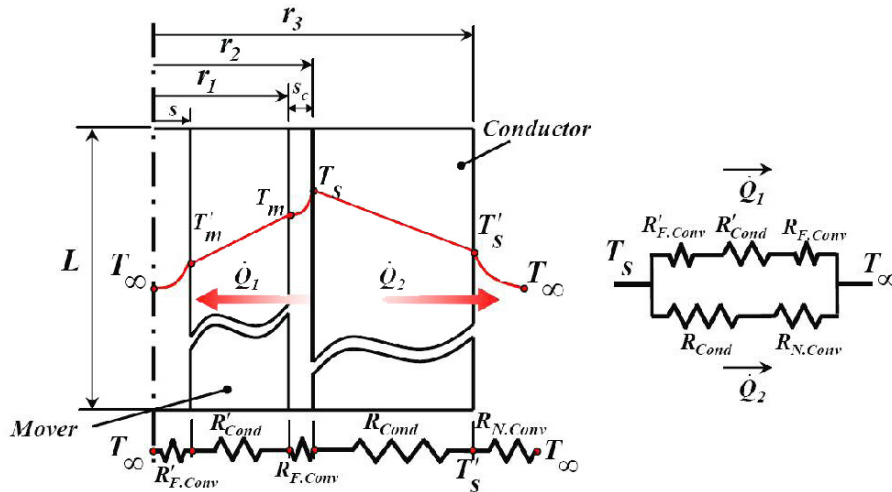


Figure 11. Thermal resistance network for heat transfer through the ECD.

Reynolds number determines the forced-convection regime (laminar/turbulent) in the air-gap. The Reynolds number inside the concentric annular ducts is calculated by

$$Re = \frac{vL_c}{\nu}, \quad (20)$$

where v and ν are the velocity and kinematic viscosity of the air, respectively. The critical Reynolds number is accepted to be 2300.

Finally, the natural-convection resistance is estimated from

$$R_{N,Conv} = \frac{1}{h_N(2\pi r_2 L)}, \quad (21)$$

h_N is the natural-convection heat transfer coefficient. A vertical cylinder can be treated as a vertical plate, when

$$2r_2 \geq \frac{35L}{Gr_L^{1/4}}, \quad (22)$$

where Gr is the Grashof number [22]; therefore, the natural-convection heat transfer coefficient is conveniently obtained from an empirical correlation equation as follows:

$$h_N = \frac{k_a}{2r_2} [2 + 0.5 (Pr Gr)^{0.25}], \quad (23)$$

where Pr is the Prandtl number of the air for the respective pressure and temperature. The Grashof number for natural convection is similar to the Reynolds number in forced convection, and is mathematically expressed as

$$Gr = \frac{g\beta(T_s - T_\infty)(2r_2)^3}{\nu^2}, \quad (24)$$

where g and β are the gravitational acceleration and coefficient of volume expansion, respectively, for an ideal gas $\beta = 1/T_\infty$. According to (23), h_N is a function of the surface temperature, so the surface temperature is obtained from (13) after a few iterations.

The properties of air at 1 atm and 20°C are $k_a = 0.0269 \text{ W m}^{-1} \text{ °C}^{-1}$, $Pr = 0.7241$, $\nu = 1.749 \times 10^{-5} \text{ m}^2 \text{ s}^{-1}$, $\beta = 1/293 \text{ K}$, and the geometry dimensions are $L = 0.1 \text{ m}$, $r_1 = 13 \text{ mm}$ and $r_2 = 25 \text{ mm}$. The aluminum-conductor and iron-mover thermal conductivities are $k_c = 235 \text{ W m}^{-1} \text{ K}^{-1}$ and $k_m = 80.4 \text{ W m}^{-1} \text{ K}^{-1}$, respectively. For the average mover velocity of 0.12 m s^{-1} , the heat transfer rate is 1.5 W . Since the Reynolds number is below the critical value, the flow regime is assumed to be laminar and the Nusselt number for the force convection is $Nu = 4.36$ [22]. The steady-state temperature rise of the conductor surface is obtained from (13) by iteration as 14.2 °C , which is within the acceptable limits.

3. Real-size ECD design

After modeling and analysis of the scaled-down ECD, the design is modified and optimized, specifically for automotive applications, achieving a higher damping performance while minimizing weight and cost. According to [15], a damper in a typical vehicle suspension system should produce an

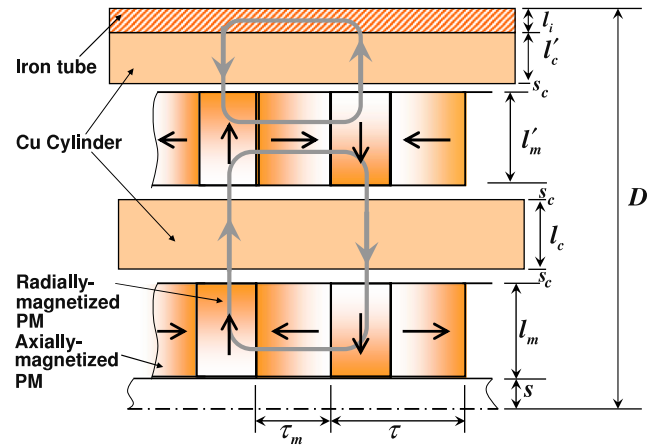


Figure 12. Schematic configuration of the real-size ECD.

RMS force value of 1040 N at the RMS damper velocity of approximately 0.8 m s^{-1} , and the maximum damper external diameter and length are 150 and 600 mm, respectively.

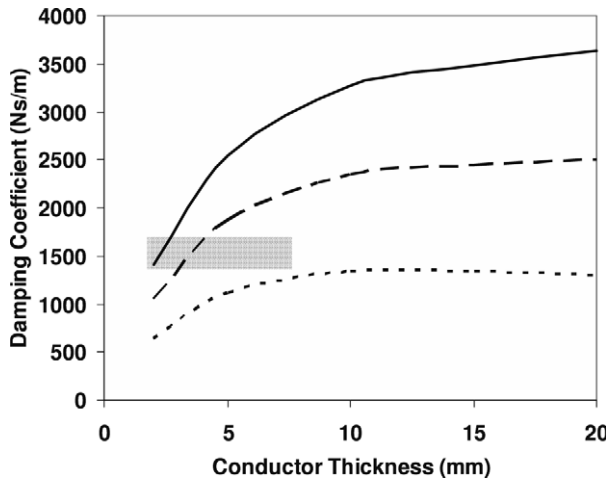
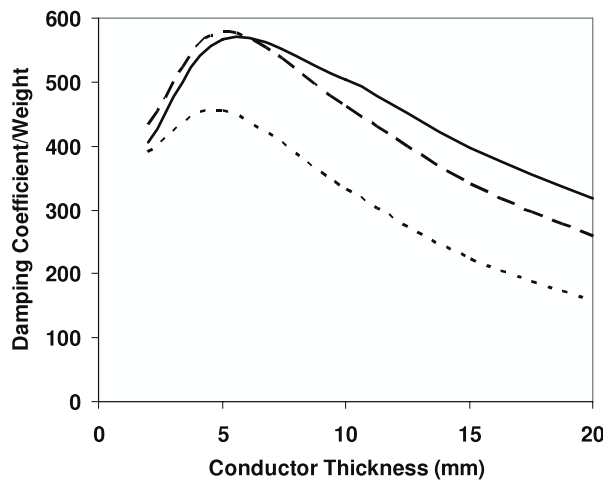
One crucial parameter in the full-size ECD design is the radial component of the magnetic flux density. According to (11), the damping force increases with the radial flux density to the second power. The research presented by Ebrahimi *et al* [23] demonstrated that using axially and radially magnetized PMs in a Halbach arrangement, as in figure 12, is the optimum configuration of PMs in the mover. Thus, a Halbach array is selected as the arrangement of PMs in the mover to augment the magnetic flux density over the conductor's length [23]. To increase the effective radial magnetic flux density over the conductor, another layer of a PM array is added to the design. Figure 12 reflects the modified ECD configuration with the additional PM tube. To take advantage of the outward magnetic flux, generated by the second PM layer, another conductor layer is added to the ECD.

Another modification is that copper is selected as the conducting material instead of aluminum because of copper's high electrical conductivity ($\sigma_{Cu} = 58.8 \times 10^6$). The outside diameter limit of the damper is set to 90 mm for the physical restriction. The design procedure for inner permanent magnets is similar to that of the scaled-down version, described in section 2.2. The air-gap thickness should be as small as possible, and is limited by the manufacturing restrictions. The air-gap thickness is set to 1 mm. The damping coefficient and the weight of the ECD for different conductor and permanent magnet thicknesses are listed in table 2. The FE method is used for the magnetic flux density estimation, and damping coefficients are calculated by integrating (4) over the conductor volume for each case.

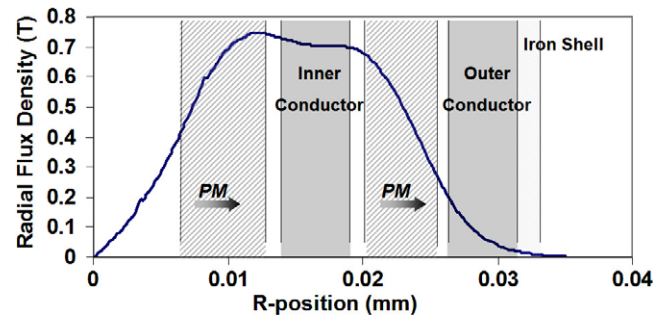
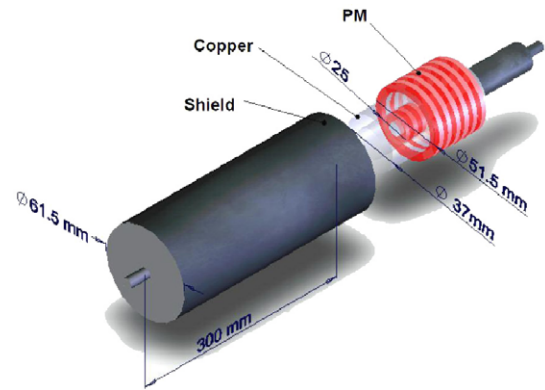
In order to obtain the optimum conductor and outer magnets' thicknesses, the generated damping coefficient for different magnet thicknesses are plotted versus the conductor thickness in figure 13. The hatched box in figure 13 shows the required passive damping coefficient [15]. It is observed that increasing the conductor thickness does not affect the damping coefficient after a certain level, and so there is an optimum conductor thickness for each outside magnets' thickness. The

Table 2. Damping coefficient and weight of the ECD for different conductor and permanent magnet thicknesses.

	$l_c = 2 \text{ mm}$	$l_c = 5 \text{ mm}$	$l_c = 10 \text{ mm}$	$l_c = 15 \text{ mm}$	$l_c = 20 \text{ mm}$
$l'_m = 3 \text{ mm}$	645 N s m ⁻¹ 1.65 kg	1118 N s m ⁻¹ 2.45 kg	1340 N s m ⁻¹ 4.03 kg	1336 N s m ⁻¹ 5.95 kg	1305 N s m ⁻¹ 8.22 kg
$l'_m = 6.25 \text{ mm}$	1053 N s m ⁻¹ 2.43 kg	1880 N s m ⁻¹ 3.25 kg	2351 N s m ⁻¹ 5.1 kg	2448 N s m ⁻¹ 7.2 kg	2498 N s m ⁻¹ 9.65 kg
$l'_m = 10 \text{ mm}$	1408 N s m ⁻¹ 3.48 kg	2551 N s m ⁻¹ 4.5 kg	3267 N s m ⁻¹ 6.48 kg	3488 N s m ⁻¹ 8.79 kg	3641 N s m ⁻¹ 11.46 kg

**Figure 13.** Damping coefficient versus conductor thickness for different outer magnet thicknesses. —: $l'_m = 10 \text{ mm}$, — —: $l'_m = 6.25 \text{ mm}$, ···: $l'_m = 3 \text{ mm}$.**Figure 14.** Damping coefficient/weight versus conductor thickness for different outer magnets' thicknesses. —: $l'_m = 10 \text{ mm}$, — —: $l'_m = 6.25 \text{ mm}$, ···: $l'_m = 3 \text{ mm}$.

amount of generated damping coefficient divided by ECD weight is also plotted in figure 14. It is revealed that the maximum damping coefficient is obtained at the conductor thickness l_c equal to 5 mm, regardless of the outer magnets' size. It is also deduced that the generated damping effect per ECD weight does not linearly increase by the outer magnets' thickness, and has its optimum value at the outer magnet thickness l'_m equal to 6.25 mm.

**Figure 15.** Radial flux density along the centerline of the radially magnetized PMs.**Figure 16.** Real-size version of the ECD for vehicle suspension systems.

After selecting the conductor and outer magnets' thicknesses, the final step is to set the outer conductor's thickness. The radial component of the magnetic flux density along the centerline of the radially magnetized PMs is shown in figure 15. Obviously, the radial flux density over the outer conductor is insignificant and its contribution to the damping force, given by (11), is less than 4% of the inner conductor. Thus, the outer conductor is omitted from the final design. Consequently, the iron shell is eliminated and replaced with a lightweight material, due to its negligible contribution in the damping coefficient enhancement.

Figure 16 offers the proposed design for a real-size ECD, consisting of a hollow copper cylinder and two cylinders of axially and radially magnetized PMs in the configuration shown in figure 12. The design specifications are listed in table 3.

Table 3. Specification of the real-size ECD.

Item/symbol	Value/unit
Number of poles p	12 poles
Pole pitch τ	20 (mm)
Magnet thickness τ_m	10 (mm)
Inner magnets	
Inside diameter $2s$	12.5 (mm)
Outside diameter $2(l_m + s)$	25 (mm)
Outer magnets	
Inside diameter $2(l_m + l_c + 2s_c + s)$	39 (mm)
Outside diameter $2(l_m + l'_m + l_c + 2s_c + s)$	51.5 (mm)
Rod diameter $2s$	12.5 (mm)
Mover mass M_m	2.25 (kg)
Outer shell thickness l_i	4 (mm)
Inner conductor	
Inside diameter $2(l_m + s + s_c)$	27 (mm)
Outside diameter $2(l_m + s + s_c + l_c)$	37 (mm)
Length	240 (mm)
Air-gap thickness s_c	1 (mm)
Damper outside diameter D	61.5 (mm)
Conductor mass M_c	1 (kg)
Damper mass $M_c + M_m$	3.25 (kg)
Magnet material	NdFeB alloy
	$B_r = 1.17$ (T)

4. Comparison and evaluation

In section 3, the optimum dimensions of the real-size ECD are derived. The evaluation of the novel ECD is followed by a comparison of the size, weight, cost and performance of four dampers: a magneto-rheological-fluid semi-active damper, two commercial passive dampers and the ECD. Table 4 illustrates the size, weight, cost and maximum damping coefficient comparison of these dampers. The passive mono-tube damper is a C1500 Chevy pickup damper that offers traditional Bilstein technology for trucks and features a single-tube high-pressure design. Another passive damper is a Tokico's D-spec series (DSP-4) damper for a Mustang, utilizing a variable-aperture bypass, which is tuned manually by an adjustable slide valve. Finally, the Cadillac MR fluid damper is a newly commercialized MagneRide damper from Delphi. The MagneRide design employs an electromagnetic coil wrapped around the passageway between the chambers, which are filled with MR fluid. The MR fluid yield stress varies through the coils' current adjustment. A comparison of the ECD with the off-the-shelf passive dampers reveals that the size and cost of the ECD is higher than those of passive oil dampers. It seems that the high density of the copper and rare earth magnets results in the ECD being three times heavier than an ordinary passive damper. Moreover, the ECD cost is more than twice as high than a commercial passive damper, due to the high cost of rare earth magnets, which is around 250 US\$ kg⁻¹.

Figure 17 illustrates the damper performance comparison. The non-dimensional damping coefficient, C/C_{\max} , is plotted for the ECD damper and compared with Mustang, Chevy [24] and Cadillac MR fluid dampers. The off-the-shelf, Cadillac, MR fluid damper is purchased and tested at different input

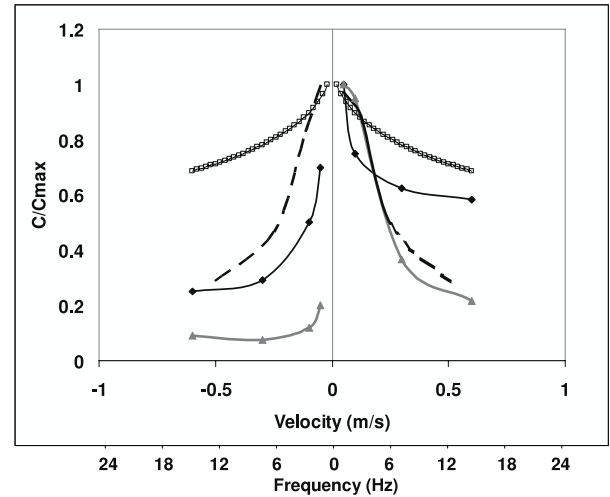


Figure 17. Normalized damping coefficient versus velocity, —▲—: Chevy pickup, —◆—: Mustang, —■—: Cadillac (0 A) and —□—: ECD.

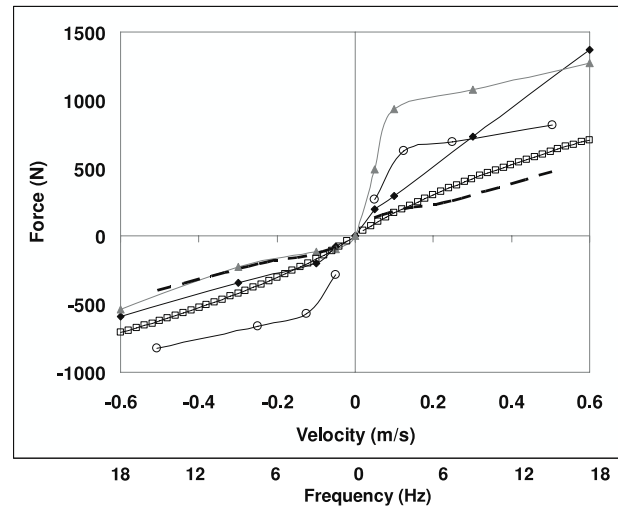


Figure 18. Force-velocity curves for different dampers, —▲—: Chevy pickup, —◆—: Mustang, —■—: Cadillac (0 A), —○—: Cadillac (1.5 A) and —□—: ECD.

currents with an MTS hydraulic shaker at the University of Waterloo. It appears that all the dampers have the same pattern of higher damping coefficients at low velocities, which is desirable in automobile damper design.

The damping performance pattern for the ECD is highly affected by the skin effect, which causes the damping to decrease at higher frequencies. In a passive suspension system, the best damping performance turns out to be a symmetrical behavior in compression and extension [25] (as in the case of ECD). However, that the asymmetrical damping performance is advantageous in the case of large disturbances stems from large potholes, by prevention of the wheel descending into the hole due to the substantial damping in extension. Figure 18 demonstrates the force-velocity curves for dampers. In compression, all dampers have the same force-velocity characteristics, except for the Cadillac MR fluid damper. For

Table 4. Size, weight, price and maximum damping comparison of dampers.

	Max. length (mm)	Weight (kg)	Cost (US\$)	C_{\max} (N s m ⁻¹) in compression	C_{\max} (N s m ⁻¹) in extension
MR fluid damper (0 A)	650	4.08	1000	1608	2642
MR fluid damper (1.5 A)	650	4.08	1000	5646	5480
Passive mono-tube damper	550	1	80	1960	9800
Passive double-tube	600	1.2	200	1568	3920
Eddy current damper	400	3.25	400	1880	1880

the MR fluid damper, the damping force increases with the applied voltage, resulting in a low damping force in the off mode. For semi-active dampers, damping performance in the off mode portrays the fail-safety of the suspension system, and the damper is required to provide an acceptable damping performance in the off mode. The poor damping characteristic in the off mode is one of the MR fluid damper's drawbacks.

In the compression mode, the ECD exhibits a higher damping force rather than other passive oil dampers. On the other hand, in extension, the ECD displays a lower force level, compared with that of other passive dampers, although its damping force is still higher than that of the MR fluid damper in the off mode.

The force–velocity curves reveal that, although the ECD force level is not so appealing in extension mode, compared with other passive dampers, it is still practical in the case for lightweight vehicles. At this stage, the performance and cost of the proposed ECD is restricted by the current magnet technology. However, with advances in magnet and conductor material technologies, the proposed system has the potential for significant improvements.

4.1. Demagnetization effect and reliability

The ECD fail-safely issue is one of the crucial factors for this feasibility study, and is highly influenced by the demagnetization of the permanent magnets in their operating life. Factors that affect the magnet stability include time, temperature, adverse fields, shock and stress. The effect of time on modern permanent magnets is minimal. Rare earth magnets are not vulnerable to the time factor due to their high coercivities. Over 100 000 h, these losses are in the range of essentially zero for the NdFeB magnets used in this study.

The heat transfer analysis in section 2.6 demonstrates that the temperature rise is far below the Curie temperature (310 °C for NdFeB) that causes the irreversible losses in the magnetization of permanent magnets. Also, the reversible loss due to the temperature rise is so small that it can be ignored. For example, in the case of NdFeB magnets in this study, the magnetization change is less than 3% for a temperature rise of 50 °C.

External magnetic fields in repulsion mode produce a demagnetizing effect as well. Rare earth magnets with coercive forces exceeding 15 kOe are not likely to be affected in this manner. The external magnetic field that should be applied to fully demagnetize a magnet depends on the coercive magnetic

field (H_c), remanent magnetization (M_r) and the shape of the magnet. For the proposed magnets' shape (cylindrical shape) the demagnetization field is equal to the remanent magnetization, so the required external magnetic field for demagnetization is obtained [21] as

$$H_{\text{ext}} = H_c - M_r. \quad (25)$$

For the rare earth magnets in this paper with $M_r = 1.03 \times 10^6$ A m⁻¹ and $H_c = 0.95 \times 10^6$ A m⁻¹, the required external field is equal to 3.7×10^5 A m⁻¹, corresponding to a magnetic flux density equal to 0.72 T, which is well beyond the effect of the adjacent magnet in the proposed configuration (where the maximum axial flux density is less than 0.4 T). Finally, the effect of shock and stress below the destructive limits are very minor on rare earth magnets. However, in the proposed configuration these effects are inconsequential due to the non-contact nature of the ECD. In conclusion, utilizing the rare earth permanent magnets in the proposed ECD ensures damper reliability and durability.

5. Conclusion

In this paper, a scaled-down passive eddy current damper (ECD) is developed by using the eddy current damping phenomenon. An analytical model for the generated damping force is derived by applying the electromagnetic equations. Then, the proposed ECD geometry is optimized and the final configuration is simulated, using FE software. Next, a scaled-down prototype ECD is fabricated and experiments done to verify the analytical model for the damping force and the magnetic flux density. In addition, a heat transfer analysis is performed for evaluating the ECD performance and ensuring that it does not overheat. Finally, after the full-size ECD is designed, based on the derived model, its performance is compared with the performances of commercial off-the-shelf dampers.

Although the weight and cost of the ECD is not very appealing, compared with commercial passive dampers, the performance of the newly developed ECD in vehicle suspension applications is still attractive. The new damper is oil-free, non-contact, offering high reliability and durability with its simplified design. The performance of the proposed ECD can be significantly improved by using high-quality, low-weight permanent magnets, and conductors with higher conductivity. Also, the novel ECD could be applicable in other

vibration isolation systems such as precision machinery and structural vibration isolation.

References

- [1] Cadwell L H 1996 Magnetic damping analysis of an eddy current brake using an air-track *Am. J. Phys.* **64** 917–23
- [2] Heald M A 1996 Magnetic braking: improved theory *Am. J. Phys.* **56** 521–2
- [3] Wiederick H H, Gauthier N, Campbell D A and Rochon P 1987 Magnetic braking: simple theory and experiment *Am. J. Phys.* **55** 500–3
- [4] Genta G, Delprete C, Tonoli A, Rava E and Mazzocchetti L 1992 Analytical and experimental investigation of a magnetic radial passive damper *Proc. 3rd Int. Symp. of Magnetic Bearings (Washington, DC, July)* pp 255–64
- [5] Sodano H, Bae J S, Inman D J and Belvin W K 2005 Concept and model of eddy current damper for vibration suppression of a beam *J. Sound Vib.* **288** 1177–96
- [6] Bae J S, Kwak M K and Inman D J 2005 Vibration suppression of cantilever beam using eddy current damper *J. Sound Vib.* **284** 805–24
- [7] Sodano H, Bae J S, Inman D J and Belvin W K 2006 Improved concept and model of eddy current damper *J. Vib. Acoust.* **128** 294–302
- [8] Teshima H, Tanaka M, Miyamoto K, Nohguchi K and Hinata K 1997 Effect of eddy current dampers on the vibration properties in superconducting levitation using melt-processed YBaCuO bulk superconductors *Physica C* **274** 17–23
- [9] Elbuken C, Khamesee M B and Yavuz M 2006 Eddy current damping for magnetic levitation: downscaling from macro to micro-levitation *J. Phys. D: Appl. Phys.* **39** 3932–8
- [10] Elbuken C, Shameli E and Khamesee M B 2007 Modeling and analysis of eddy-current damping for high-precision magnetic levitation of a small magnet *IEEE Trans. Magn.* **43** 26–32
- [11] Schmid M and Varga P 1992 Analysis of vibration-isolating systems for scanning tunneling microscopes *Ultramicroscopy* **42–44** 1610–15 Part B
- [12] Tonoli A 2007 Dynamic characteristics of eddy current dampers and couplers *J. Sound Vib.* **301** 576–91
- [13] Graves K E, Toncich D and Iovenitti P G 2000 Theoretical comparison of motional and transformer EMF device damping efficiency *J. Sound Vib.* **233** 441–53
- [14] Ebrahimi B, Khamesee M B and Golnaraghi M F 2008 Design and modeling of a magnetic shock absorber based on eddy current damping effect *J. Sound Vib.* **315** 875–89
- [15] Martins I, Esteves J, Marques G D and Pina da Silva F 2006 Permanent-magnet linear actuators applicability in automobile active suspensions *IEEE Trans. Veh. Technol.* **55** 86–94
- [16] Chaves M, Martins I, Maia J and Esteves J 2003 Experimental implementation of an electromagnetic, automobile suspension system *Proc. 11th Mediterranean Conf. on Control and Automation* p 5
- [17] Foito D, Esteves J and Maia J 2003 Experimental and simulation results of an electric vehicle *Proc. 11th Mediterranean Conf. on Control and Automation* p 5
- [18] Mirzaei S 2007 A flexible electromagnetic damper *IEMDC 2007: Proc. IEEE Int. Electric Machines and Drives Conf.* pp 959–62
- [19] Forbes L K, Cozier S and Doddrell D M 1997 Rapid calculation of static fields produced by thick circular solenoids *IEEE Trans. Magn.* **33** 4405–10
- [20] Craik D 1995 *Magnetism: Principles and Applications* (New York: Wiley) pp 334–6
- [21] Furlani E P 2001 *Permanent Magnet and Electromechanical Devices, Materials, Analysis and Applications* (San Diego: Academic) pp 126–30
- [22] Cengel Y and Turner R 2005 *Fundamentals of Thermal-Fluid Sciences* 2nd edn (New York: McGraw-Hill)
- [23] Ebrahimi B, Khamesee M B and Golnaraghi F 2008 Permanent magnet configuration in design of an eddy current damper [doi:10.1007/s00542-008-0731-z](https://doi.org/10.1007/s00542-008-0731-z)
- [24] Vahid O 2006 Experimental investigation of a variable damper *Mechworks Systems Inc.* Document file number: 060115-1, January
- [25] Thompson A G 1969 Optimum damping in a randomly excited non-linear suspension *Proc. Inst. Mech. Eng.* 2A **184** 169–78